

Polar Sea Ice Mapping Using SeaWinds Data

Hyrum S. Anderson and David G. Long

Brigham Young University, Microwave Earth Remote Sensing Laboratory
459 CB, Provo, UT 84602 801-422-4884, FAX: 801-422-0201 hsanders@ee.byu.edu, long@ee.byu.edu

Abstract- Microwave remote sensing provides an excellent means for mapping polar sea ice extent. In this study, a new algorithm for polar sea ice mapping is developed for use with the SeaWinds instrument. The approach utilizes *a priori* information within the framework of Bayes detection to produce sea ice extent maps. Statistical models for sea ice and ocean are represented in histograms which are filtered using a principal component (PC) based filtering technique. Spatial *a priori* information is incorporated through the loss terms associated with Bayes risk. Sea ice extent maps produced by the algorithm correlate well with the Remund-Long algorithm.

I. INTRODUCTION

The ability to monitor the extent and type of polar sea ice has been enhanced through the use of microwave scatterometers because of their independence of solar illumination, their ability to penetrate to ever-present canopy of clouds in the polar regions, and the high spatial and temporal resolution of the data. Several studies have verified the utility of microwave scatterometer data in polar sea ice classification, including the Remund-Long (RL) sea ice extent algorithm [1] for SeaWinds—used operationally by NOAA for sea ice monitoring and at JPL for use in wind retrieval.

In this document, a sea ice mapping algorithm is developed using data derived from the SeaWinds instrument aboard QSCAT. A classification scheme is developed within the framework of Bayes detection such that spatial and statistical *a priori* data may be incorporated.

II. BACKGROUND

The SeaWinds instrument was launched aboard QuikSCAT (QSCAT) in June 1999 to fill the Ku-band data gap left by the failure of the NSCAT. The SeaWinds instrument measures v-pol σ^o at 54° incidence, and h-pol σ^o at 46° incidence. The outer beam forms an 1800-km swath and the inner beam forms a 1400-km swath, each with no nadir gap. The instrument covers 100% of the polar regions each day, excepting a gap directly over the poles due to the orbit geometry.

The SeaWinds instrument operates in two spatial resolution modes [2]. The intrinsic elliptical measurement cells, called “eggs” have nominal resolution of 24-km in azimuth by 37-km in the range direction. Egg data is used in this study.

A. Backscatter Images

To grid the SeaWinds data, and to increase the nominal sensor resolution, the Scatterometer Image Reconstruction (SIR) algorithm [3] is used. SIR combines data from multiple satellite swaths to enhance the resolution of the backscatter images.

SeaWinds egg imagery gridded using the SIR algorithm is enhanced to 4.45 km pixel resolution, with an effective resolution of 8–10 km.¹

The SIR algorithm produces several image products derived from the SeaWinds instrument, including A_v , A_h , V_v , and V_h . A_v and A_h are the enhanced resolution σ^o images for v-pol and h-pol, respectively. Each pixel represents an “average” σ^o measurement over the 24-hour interval from multiple swaths and from multiple looks in the same swath (i.e., azimuthal modulation contributes to the average). V_v and V_h are v-pol and h-pol standard deviation estimates of these same measurements.

The A imagery exhibits good statistical contrast between sea ice and ocean—rough surface scattering and volume scattering in sea ice contribute to an overall higher backscatter over sea ice than over the ocean, for which surface scattering dominates. The V imagery also exhibits contrast because σ^o measurements of the ocean show high temporal variability between successive satellite swaths and are affected by azimuth modulation from ocean waves. These effects are relatively small over sea ice, which exhibits lower diurnal variations and greater isotropy.

The co-polarization ratio (PR) is defined to be the ratio (difference in log-space) of A_v and A_h . PR couples two microwave dependencies: incident angle dependence, and polarization dependence. Measurements of σ^o from sea ice backscatter show smaller incident angle dependence than ocean due to rough surface and volume scattering. In addition, σ^o measurements of ocean exhibit a v-pol bias, unlike σ^o measurements of sea ice.

III. MODIFIED BAYES DETECTION ALGORITHM

Four SIR image products—PR (derived), A_h , V_v , and V_h —are used in concert as discrimination parameters to detect sea ice. Since it is helpful to incorporate *a priori* information in an estimate of polar sea ice extent, the algorithm is developed within the framework of Bayes detection, where a decision rule $\phi(\mathbf{z})$ selects sea ice or ocean based on an observation \mathbf{z} , and depending on the Bayes risk $R(\cdot)$ associated with that decision,

$$\phi(\mathbf{z}) = \begin{cases} \text{sea ice,} & \text{if } R(\text{sea ice}|\mathbf{z}) < R(\text{ocean}|\mathbf{z}) \\ \text{ocean,} & \text{otherwise.} \end{cases} \quad (1)$$

The algorithm is designed for pixel-based classification, in which observations $\mathbf{z} = [\text{PR } A_h \ V_v \ V_h]$ for each pixel at position (x, y) and time t are used to determine the Bayes risk,

¹SIR science data products are available at the Scatterometer Climate Pathfinder website, <http://www.scp.byu.edu>.

which is related to the probability $P(\cdot)$ that a hypothesis $H_i^{x,y,t}$ (the pixel belongs to class i) is correct given the observation \mathbf{z} . The decision rule selects the hypothesis ($H_1^{x,y,t}$ for sea ice and $H_0^{x,y,t}$ for ocean) which results in a minimum Bayes risk,

$$R(H_i^{x,y,t}|\mathbf{z}) = P(H_i^{x,y,t}|\mathbf{z})L_{ij}^{x,y,t}, \quad (2)$$

where $L_{ij}^{x,y,t}$ is an arbitrarily assigned loss for selecting $H_i^{x,y,t}$, given that $H_j^{x,y,t}$ is correct. In practice, it is difficult and sometimes impossible to calculate the probability in Equation (2) for every pixel. In image processing, a common practice is to treat the pixel statistics as ergodic, i.e., the pixel statistics are approximately equal to the ensemble statistics. With this simplification, but retaining the general form for the loss, Equation (2) reduces to

$$R(H_i^{x,y,t}|\mathbf{z}) = P(H_i^t|\mathbf{z})L_{ij}^{x,y,t}. \quad (3)$$

In this form, inaccuracy introduced by neglecting spatial dependence in the $P(H_i^t|\mathbf{z})$ may be accounted for by careful selection of $L_{ij}^{x,y,t}$.

Equation (3), written in terms of the *posteriori* probability, may expressed in terms of the *a priori* probability using Bayes theorem. To facilitate a binary decision (sea ice or ocean) using a likelihood ratio test, Bayes risk is expressed in terms of a conditional distribution [4]. This results in an effective decision rule $\phi(\mathbf{z})$ for an observation \mathbf{z} ,

$$\phi(\mathbf{z}) = \begin{cases} 1, & \text{if } f(\mathbf{z}|H_1^t)P(H_1^t)L_{10}^{x,y,t} > \\ & f(\mathbf{z}|H_0^t)P(H_0^t)L_{01}^{x,y,t} \\ 0, & \text{otherwise,} \end{cases} \quad (4)$$

where 1 represents sea ice and 0 represents ocean. The decision threshold is adjusted by the priors and the costs associated with the decision. Rather than selecting a functional form for $f(\mathbf{z}|H_i^t)$, the conditional distributions are approximated using histograms (un-normalized) to allow for temporal variations of sea ice and ocean. Equation (4) becomes

$$\phi(\mathbf{z}) = \begin{cases} 1, & \text{if } h(\mathbf{z}|H_1^t)L_{10}^{x,y,t} > h(\mathbf{z}|H_0^t)L_{01}^{x,y,t} \\ 0, & \text{otherwise.} \end{cases} \quad (5)$$

Note that the prior probabilities are reflected in the relative heights of the histograms.

The Bayes detection formulation in Equation (5) allows for a simple pixel-based test of ensemble sea ice and ocean histograms (4-dimensional), where the loss terms essentially shift the threshold of the decision.

A. Loss Maps

The value assigned to $L_{ij}^{x,y,t}$ can be arbitrarily chosen and, in practice, is used to reflect the *a priori* belief that the hypothesis $H_i^{x,y,t}$ is correct. The relative values of the loss terms in the decision rule of Equation (5) shift the decision threshold by

scaling the histograms. Using $L_{ij}^{x,y,t}$ as a measure of prior belief, we may relate it to the probability that the observed pixel belongs to class i , given that it belonged to class j yesterday; in effect,

$$L_{ij}^{x,y,t} \sim P(H_i^{x,y,t}|H_j^{x,y,t-1}). \quad (6)$$

We implement $L_{ij}^{x,y,t}$ as a look-up table that retrieves a loss value for pixel location (x, y) . For sea ice mapping, we set $L_{ij}^{x,y,t}$ based on sea ice extent maps from the previous day. Since the ice edge may move several kilometers in a single day, and the sea ice extent map from the previous day may over- or under-represent the true sea ice edge, we allow for sea ice growth and imperfect sea ice maps.

The ratio of the loss maps $L_{01}^{x,y,t}/L_{10}^{x,y,t}$ adjusts the threshold for the decision rule in Equation (5). This ratio determines the classification result if the bin heights of $h(\mathbf{z}|H_1^t)$ and $h(\mathbf{z}|H_0^t)$ for an observed \mathbf{z} are equal. The dilation procedures used in forming the loss maps create a region where equal loss is assigned to both sea ice and ocean. In this region of ignorance where $L_{01}^{x,y,t} = L_{10}^{x,y,t}$ (where spatial *a priori* information is inconclusive), the unweighted ratio of the sea ice and ocean histograms determines the classification.

B. Iterative Bayes Detection Algorithm

The Bayes detection approach is used iteratively to produce polar sea ice extent maps from SeaWinds data. First, an initial estimate of sea ice extent is produced using histograms for sea ice and ocean from the previous day. Loss maps $L_{01}^{x,y,t}$ and $L_{10}^{x,y,t}$ are generated from ice extent maps from the previous day. Here, it is assumed that the statistics and spatial distribution for sea ice and ocean do not change significantly in a single day, except for sea ice growth and retreat in the region of ignorance.

Since sea ice and ocean statistics and spatial distributions do, however, exhibit diurnal variations, this initial estimate generally contains classification errors. To reduce the number of misclassified pixels, the initial classification is used to generate statistical and spatial information for another iteration of the classifier. This process is repeated until convergence.

Since initial loss maps $L_{01}^{x,y,t}$ and $L_{10}^{x,y,t}$ are constructed to allow for sea ice growth/retreat, the region of ignorance around the sea ice edge may be large. As noted previously, the loss maps do not influence the decision rule within this region. This can result in misclassifications if the discrimination parameters exhibit microwave signature anomalies within the region. To increase the efficacy of the loss maps as the algorithm nears convergence, the loss maps are updated at each iteration to reflect the new sea ice location from the most recent classification. Also, the loss maps are updated at each iteration so that the region of ignorance contracts. This is accomplished

through a simple simulated annealing update step,

$$\hat{L}_{01}^{x,y,t} \leftarrow (1 - \alpha) \hat{L}_{01}^{x,y,t} + \alpha L_{ij}^{x,y,t} \quad (7)$$

$$\alpha \in [0, 1]$$

where α is a forgetting factor, $\hat{L}_{01}^{x,y,t}$ is the adaptive position-conformal loss map, and $L_{ij}^{x,y,t}$ is a loss map created from the classification results of each iteration. To force the region of ignorance to contract, each new loss map $L_{ij}^{x,y,t}$ in the iteration sequence is created using fewer dilations of the sea ice classification map than the loss map of the previous iteration. The initial loss map is created from an estimate of sea ice extent from a previous day, as described previously, using the most number of dilations.

A diagram detailing the flow of the algorithm is shown in Figure 1. A sample sea ice extent map for the Arctic region is shown in Figure 2.

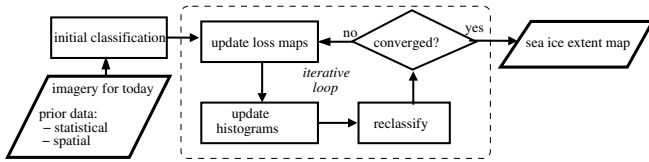


Fig. 1. Flowchart of the sea ice mapping algorithm

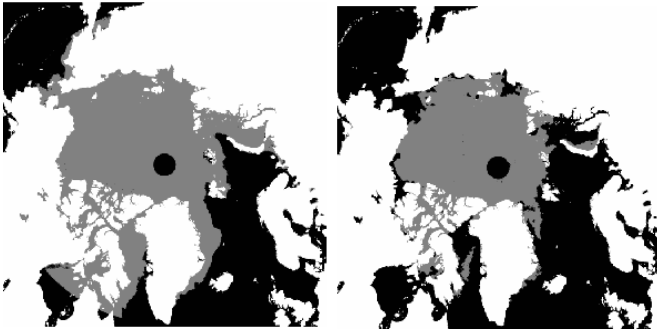


Fig. 2. Sample output of the sea ice mapping algorithm. Prior data was obtained via an ice extent map produced by the RL algorithm. Shown are the ice maps for JD 6, 2001 (left) and JD 206, 2001 (right). Note that the ice maps are truncated south of the 45th parallel.

IV. RESULTS

Results from the modified Bayes algorithm are compared to results from the RL algorithm for SeaWinds. Figure 3 shows the resulting sea ice areas reported by both algorithms for the Arctic region (from the pole south to 45° N latitude). The algorithms report similar ice areas, but are marked by two major distinctions in the figure. Since the new approach does include a binary filtering stage, it is capable of tracking sections of sea ice disjoint from the main ice sheet. The new approach also shows greater temporal consistency by virtue of the spatial *a priori* information in the loss maps. This is evidenced in the Figure 3 by surface melting in the lower latitudes that is not corrected by the RL algorithm (JD 125–160). The discrepancy from JD 200–270 is caused by higher-latitude melt events which are corrected in the binary processing phase of the RL algorithm.

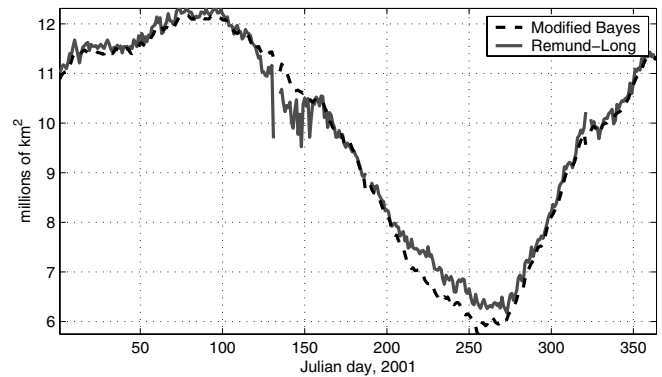


Fig. 3. Comparison of total ice area reported by the modified Bayes and RL algorithms for SeaWinds.

REFERENCES

- [1] Q.P. Remund and D.G. Long, "Sea ice mapping algorithm for QuikSCAT and SeaWinds", *Proceedings of the International Geoscience and Remote Sensing Symposium*, vol. III, pp. 1686–1688, July 1998.
- [2] T. Lungu, Ed., *QuikSCAT Science Data Product User's Manual*, Jet Propulsion Laboratory, Pasadena, CA, 2001.
- [3] D.G. Long, P. Hardin, and P. Whiting, "Resolution enhancement of spaceborne scatterometer data", *IEEE Transactions on Geoscience and Remote Sensing*, vol. 31, pp. 700–715, 1993.
- [4] T.K. Moon and W.C. Stirling, *Mathematical methods and algorithms for signal processing*, Prentice-Hall, Upper Saddle River, NJ, 2000.